

Performance Parameters of Infra-red and Visible-active MXene Photocatalysts for Water Splitting

Swati Shaw* and Subhradip Ghosh†

Department of Physics, Indian Institute of Technology Guwahati, Guwahati-781039, Assam, India.

Water splitting reactions through photocatalysis is an efficient and sustainable technique for the generation of green energy. The photocatalyst's ability to effect simultaneous generation of hydrogen and oxygen, along with efficiency in utilisation of charged carriers, conversion of solar energy to hydrogen, fast migration, and low recombination rates of carriers, are the parameters to decide its suitability in water splitting. In literature, comprehensive calculation and analysis of all these performance parameters for a potential photocatalyst are rare. In this work, we have performed first-principles-based computations to find new efficient photocatalysts from the family of Janus MXenes and assessed their performance parameters. Strain engineering has been invoked in search of new materials. Out of 14 studied materials, we find 5 materials: Sc_2COS , Zr_2COS , Hf_2COS , and ZrHfCO_2 under zero or finite tensile strain and Hf_2COSe at 6% tensile strain meeting the requirements of simultaneous reactions to split water. The computations of various efficiency-related parameters demonstrate that Zr_2COS , Hf_2COS , and Hf_2COSe have excellent efficiencies, significantly better than the well-known photocatalysts. The origin of such performances lies in their electronic and optical properties, which are analysed systematically.

I. INTRODUCTION

Photocatalytic water splitting is one of the sustainable techniques for utilising solar energy to produce hydrogen. Economic production of hydrogen from sunlight via photocatalytic splitting of water requires at least 10 % solar-to-thermal (STH) efficiency [1, 2]. The STH efficiency depends on light harvesting, separation of carriers, their transportations, hydrogen evolution reactions (HER), and oxygen evolution reactions (OER). To increase the STH efficiency through these steps requires a photocatalyst with an electronic band gap of at least 1.23 eV so that it is greater than or equal to the energy difference between $\text{H}_2\text{O} \rightarrow \text{O}_2$ (OER) and $\text{H}^+ \rightarrow \text{H}_2$ (HER) reactions. The alignment of the band edges, the optical absorbance, the carrier mobilities, and the binding energy of excitons contribute to this. Assuming 100% light absorption and quantum efficiency, the theoretically calculated maximum STH efficiency is about 48% [3]. However, energy loss due to carrier migration and separation of bound electron-hole pairs is unavoidable. Substantial overpotentials are also required to drive the reactions. Factoring these in, the realistic potential required to drive the photocatalytic process is generally greater than 2.0 V [4]. This implies that the band gap

of the photocatalyst should be around 2.0 eV, resulting in absorption of only 8% of the solar spectrum, coming mostly from the ultra-violet (UV) part. This reduces the theoretical STH efficiency to $\sim 18\%$ only [4, 5]. Many attempts [6–10] have been made to improve the STH efficiency that put the choice of material as photocatalyst at the centerstage.

Enhancement in the STH efficiency is possible if light from the Infrared (IR) region is absorbed as it accounts for nearly 50% of the solar energy. This requires doing away with the constraint on the electronic band gap of the catalyst material. A proposed mechanism that exploits the presence of an intrinsic electric field along z -direction to lift the restriction on band gap [11] has led to the prediction of several new IR active photocatalysts from the family of two-dimensional (2D) materials [12–14]. 2D materials, due to their high surface to volume ratio, a large number of surface reactive sites, excellent optical absorption, high carrier mobility, faster carrier transfer, and low recombination rates, are ideal for catalysing photo-assisted water splitting. These traits, along with the possibility of creating a vertical internal electric field that may enable tapping the IR part of the solar spectrum, project them as ideal compounds to amplify STH efficiency in photocatalytic water splitting. Among them, M_2X_3 ($\text{M}=\text{Al}, \text{Ga}, \text{In}$; $\text{X}=\text{S}, \text{Se}, \text{Te}$) turn out to be substantially efficient in solar to hydrogen conversion as several compounds in the series have STH greater than 10% [5]. For example, IR light-

* swatishaw@iitg.ac.in

† subhra@iitg.ac.in

driven photocatalyst In_2Te_3 , in this series, has a large STH efficiency of 32 %. Another prominent family of 2D compounds that exhibit both OER and HER simultaneously is the Janus transition metal di-chalcogenides [12, 15–21]. These compounds have higher STH along with higher carrier mobility compared to their parent compounds. The two reactions associated with water splitting can take place on two surfaces of these compounds, leading to fast carrier transport.

MXenes with chemical formula $\text{M}_{n+1}\text{X}_n\text{T}_n$ (M a transition metal, X carbon or nitrogen and T a functional group like -O, -F, -S, -Se), a relatively new addition to the family of 2D compounds, has turned out to be a family of compounds where the compositional flexibility can be utilised to obtain a variety of superior functional properties [22–32]. Apart from predicting several M_2CT_2 MXenes as potential photocatalysts for water splitting [33–35] by Density Functional Theory (DFT) calculations, possibility to obtain new photocatalysts has been explored by constructing Janus MXenes where either T or M on the two surfaces of $n = 1$ MXene are different [36–41]. In a recent DFT based combinatorial study on 47 Janus $\text{M}_2\text{CTT}'$ and $\text{MM}'\text{CT}_2$ MXenes [42] four new potential photocatalysts, two IR active and two visible light active, are predicted. Out of these, IR active Zr_2COS , Hf_2COS and visible light active Sc_2COS belong to the sub-family of M_2COT where $\text{M} = \text{Sc}, \text{Ti}, \text{Zr}, \text{Hf}$ and $\text{T} = \text{S}, \text{Se}$. ZrHfCO_2 , the other visible light active photocatalyst belongs to the sub-family of $\text{MM}'\text{CO}_2$ ($\text{M}, \text{M}' = \text{Sc}, \text{Ti}, \text{Zr}, \text{Hf}$). In course of this investigation, it was discovered that Sc_2COSe from M_2COT family and TiZrCO_2 , TiHfCO_2 from $\text{MM}'\text{CO}_2$ family are semiconductors where due to inappropriate position of valence band maxima (VBM) only HER can take place. Moreover, Ti_2COS , Ti_2COSe , Hf_2COSe , Zr_2COSe from M_2COT sub-family and ScTiCO_2 , ScZrCO_2 , ScHfCO_2 from $\text{MM}'\text{CO}_2$ group of compounds are semi-metals. Since strain engineering is a well-known cheap way of modulating the band structure of a material, the application of external strain in these compounds may induce semiconducting gap opening in the semi-metals and proper alignments of band edges in the semiconductors, resulting in new catalysts for photo-assisted water splitting. Moreover, the overpotentials associated with the HER in Zr_2COS and Hf_2COS are about 0.1 eV only, while those associated with the OER in Sc_2COS is 0.14 eV. For ZrHfCO_2 , the overpotentials associated with both reactions are about 0.25 eV. The application

of strain can be a useful way to enhance these overpotentials.

None of the works on MXenes available so far considered calculations of the STH efficiency. Another important component to assess the performance of a proposed photocatalyst, the exciton binding energy, is also missing in those works. The coulomb interaction between photo-excited electrons and hole pairs is attractive resulting in excitons, a quasiparticle bound state. The lower the exciton binding energy, the easier the separation of the carriers with opposite charges. This lowers the probability of recombination and thus increases the performance of the photocatalyst. In this work, we address these issues by performing first-principles DFT-based calculations on the above-mentioned 14 Janus MXenes under bi-axial compressive and tensile strains. Apart from the four photocatalysts already predicted, we find Hf_2COSe under 6% tensile strain to be a new IR active photocatalyst. We find significant improvement of overpotentials in Zr_2COS and Hf_2COS under strain. The calculations of optical spectra, STH efficiency, and exciton binding energies are carried out. The results indicate that Zr_2COS , Hf_2COS , and Hf_2COSe have excellent performance parameters and can be considered as useful IR active photocatalysts for water-splitting. ZrHfCO_2 , on the other hand, has reasonably good performance parameters and can be useful as a visible active photocatalyst.

II. COMPUTATIONAL DETAILS

DFT with Projector Augmented Wave-Pseudopotential (PAW-PP) basis [43, 44] as implemented in Vienna *ab initio* simulation package (VASP) [45, 46] has been used in this work. The Perdew-Burke-Ernzerhof (PBE) parametrisation of Generalized Gradient Approximation (GGA) is used to approximate the exchange-correlation part of the Kohn-Sham Hamiltonian. Plane waves up to 550 eV are considered. The convergence thresholds for Hellmann-Feynman force and total energy are chosen as 10^{-3} eV/Å and 10^{-6} eV, respectively. A Γ -centered k -point grid of $9 \times 9 \times 1$ is used for geometry optimization. A 20 Å vacuum slab is inserted along the z -direction to minimize the interaction between adjacent layers. The more accurate Heyd-Scuseria-Ernzerhof (HSE06) [47] hybrid functional with dipole correction along z direction is used to calculate electronic band structures. The elastic

constants are obtained using a stress-strain relation with five different distortions of the lattice.

The dynamical stability of a system is investigated by computing the phonon dispersions. Density Functional Perturbation Theory method [48] as implemented in PHONOPY code [49] is used to compute phonon spectra. Phonon calculations are performed in a $4 \times 4 \times 1$ supercell with a Γ centered $3 \times 3 \times 1$ k -mesh. *Ab initio* molecular dynamics (AIMD) simulations are done to check the thermal stability of systems. The calculations are done with $3 \times 3 \times 1$ supercells at room temperature (300K). Nose-Hoover thermostat [50] is used. Simulations are run up to 15 ps with a time step of 2 fs. The optical absorption spectra are obtained by computing frequency-dependent dielectric functions using HSE06 functional where the Brillouin Zone is sampled with a $9 \times 9 \times 1$ k -grid.

III. RESULTS AND DISCUSSIONS

As it has been mentioned earlier, 14 Janus MXenes, 8 from M_2COT family and 6 from $MM'CO_2$ family have been considered in this work. Biaxial strain defined as $\alpha = \left(\frac{a - a_0}{a_0} \right) \times 100\%$, where $a(a_0)$ is the lattice constant of the strained (unstrained) Mxene monolayers, has been applied on them. $\alpha > (<)0$ implies tensile(compressive) strain. α is varied from -4 to 6(-3 to 5)% for $M_2COT(MM'CO_2)$ compounds.

A. Mechanical, Dynamical and Thermal Stabilities of the Compounds

Before investigating the effects of strain on the band structure and other properties directly associated with the photocatalyst's utility, it is important to make sure the compounds are stable under applied strain. To this end, we first look at the mechanical stability of the MXenes considered. This is done by calculating their elastic moduli at the respective equilibrium volumes. We have computed the three elastic constants C_{11}, C_{12} and $C_{66} = \left(\frac{C_{11} - C_{12}}{2} \right)$ and derived Poisson's ratio $\nu = \frac{C_{12}}{C_{11}}$ and Young's Modulus $Y = \left(\frac{C_{11}^2 - C_{12}^2}{C_{11}} \right)$ from them. The results are presented in Table S1, supplementary information. We apply the Born-Huang's criteria $C_{11} > 0, C_{11} > |C_{12}|, C_{66} > 0$ to assess mechanical stability. All 14 compounds investigated satisfy the

criteria and are, therefore, mechanically stable.

The dynamical stability is examined by computing phonon dispersion relations of the compounds by varying α . The results are shown in Figures S1-S3, supplementary information. Among the MXenes in M_2COT series, all except Ti_2COSe are dynamically stable with strain between -4 % and 4%. Ti_2COSe is stable at compressive strain only. On the other hand, Hf_2COS and Hf_2COSe have no imaginary modes even upto $\alpha = 6\%$, the highest strain applied. Among the $MM'CO_2$ compounds, only $ScZrCO_2$, $ScHfCO_2$ and $ZrHfCO_2$ have stable phonon modes for the entire range of strain ($\alpha = -3\%$ to 5%). $ScTiCO_2$ is dynamically stable upto 3% strain while $TiZrCO_2$ and $TiHfCO_2$ maintain their stability only upto a strain of 1%. The results suggest that the presence of Zr/Hf as one of the transition metals provides a greater range of stability in Janus MXenes. The thermal stability of each one of these MXenes at room temperature is then assessed by looking at the variations in their temperature and free energy with simulation run time. The calculations are done only at the highest value of α , where the systems are dynamically stable. The results are shown in Figures S1-S3, supplementary information. We find that all the structures except $ScTiCO_2$ remain intact at this temperature and strain, indicating thermal stability in all of them. $ScTiCO_2$, although it is dynamically stable up to 3% of tensile strain, the structure is thermally stable up to only 1% strain. For subsequent calculations, we have considered only the range of α where each one of the compounds is dynamically stable.

Therefore, -4% to 4% strains are applicable on Sc_2COS , Sc_2COSe , Zr_2COS , Zr_2COSe and Ti_2COS except Ti_2COSe , whereas -4% to 6% strains on Hf_2COS & Hf_2COSe . In the case of $TiZrCO_2$ and $TiHfCO_2$, we will use up to 1% strain and for $ZrHfCO_2$ up to 5% tensile strain for upcoming calculations.

B. Electronic Band Structures and Alignment of Band Edges

The motivation behind strain engineering in this work is to modulate the band structures so that a semiconducting gap opens in the Janus MXenes that are semi-metals without strain and the alignments of conduction band minima (CBM) and valence band maxima (VBM) align appropriately in compounds that are semiconductors in their equilibrium volume as well as

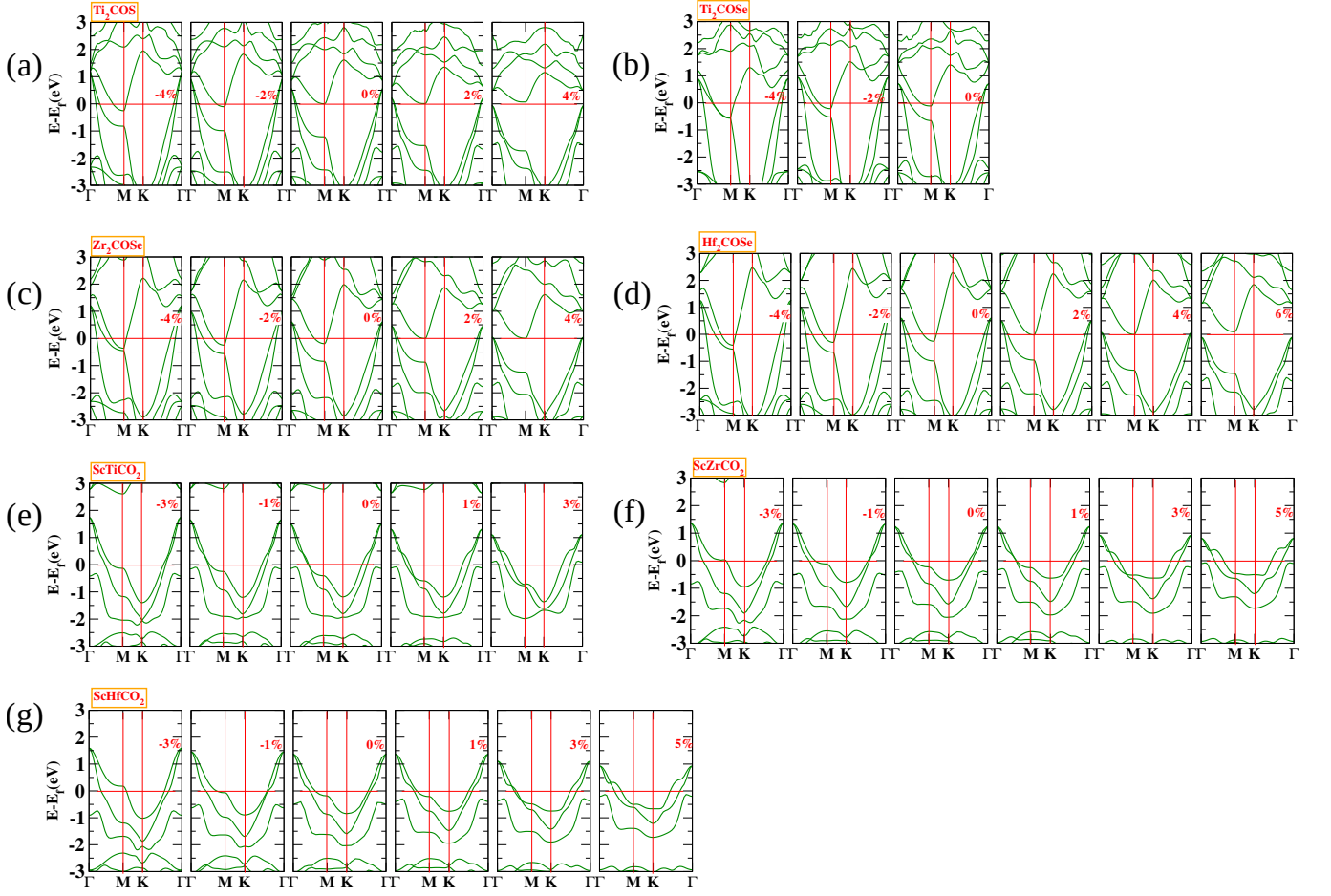


FIG. 1: The Electronic Band Structures of a) Ti_2COS , b) Ti_2COSe , c) Zr_2COSe , d) Hf_2COSe , e) ScTiCO_2 , f) ScZrCO_2 and g) ScHfCO_2 under various Biaxial strains. The Fermi level is marked with a horizontal red line.

in the ones that become semiconductors under strain. In Figure 1 (Figure S4, supplementary information), we present the results on electronic band structures as a function of the strain of the Janus compounds that are semi-metals(semiconductors) at equilibrium, that is, with $\alpha = 0$. The tensile strain of 4% (6%) opens a semiconducting gap of 0.12 (0.2) eV in Ti_2COS (Hf_2OSe). The other 5 semi-metals remain metallic even after being subjected to a sizeable strain. In both cases, the semiconducting gaps are indirect with VBM at Γ and CBM at M-point. The 7 semiconducting Janus MXenes remain semiconductors under tensile strain. Compressive strain of 4% induces semiconductor-metal transition in Zr_2COS and Hf_2COS only (Figure S4(c),(d), supplementary information). For these 7 compounds, the locations of CBM and VBM in the Brillouin zone do not change with strain; the only change is in the size of the electronic band gap. From Table I, we find that while band gap E_g in $\text{MM}'\text{CO}_2$ MXenes increases monotonically with α , it is

not so for the M_2COT MXenes. The compressive strain drastically decreases E_g in Zr_2COS and Hf_2COS turning them almost metallic at 2% strain. This explains their transformation to metal upon further increase in compressive strain. The trend of decrease in E_g with an increase in compressive strain is also observed in Sc_2COSe and Sc_2COS . Since E_g in these compounds are about 2-2.6 eV when no strain is applied, no dramatic change in electronic state is obtained when they are subjected to compressive strain. With tensile strain, the band gaps in Zr_2COS and Hf_2COS increase monotonically. The trend is opposite for the two Sc_2COT MXenes. In spite of its increase with α , the maximum E_g of IR-active Zr_2COS and Hf_2COS are about 1.0 eV. This suggests that these two MXenes can continue to be IR-active under tensile strain.

To understand the trends in the band gap E_g with α and to find out how strain modulates the positions of VBM and CBM, in Figure 2, we show the band edge po-

TABLE I: Variations in the Electronic Band Gap (E_g), Electrostatic Potential Difference ($\Delta\Phi$) between two surfaces, HER Overpotential ($\chi(H_2)$) and OER Overpotential ($\chi(O_2)$) with Biaxial strain α .

Compounds	α (%)	E_g (eV)	$\Delta\Phi$ (eV)	$\chi(H_2)$ (eV)	$\chi(O_2)$ (eV)	Compounds	α (%)	E_g (eV)	$\Delta\Phi$ (eV)	$\chi(H_2)$ (eV)	$\chi(O_2)$ (eV)
Sc ₂ COS	-4	2.57	0.73	2.06	0.02	Sc ₂ COSe	-4	1.62	0.64	1.86	-0.83
	-2	2.64	1.20	2.52	0.09		-2	1.90	1.13	2.48	-0.68
	0	2.57	1.58	2.78	0.14		0	1.97	1.52	2.81	-0.55
	2	2.44	1.88	2.92	0.18		2	1.91	1.82	2.94	-0.44
	4	2.28	2.13	2.99	0.20		4	1.82	2.07	3.00	-0.35
Zr ₂ COS	-2	0.04	1.54	-0.31	0.66	Hf ₂ COS	-2	0.01	1.44	-0.28	0.50
	0	0.36	1.78	0.05	0.86		0	0.35	1.70	0.09	0.73
	2	0.63	1.94	0.35	0.98		2	0.66	1.86	0.38	0.91
	4	0.86	2.10	0.62	1.11		4	0.90	2.02	0.64	1.05
Ti ₂ COS	4	0.12	1.17	-0.37	0.44	Hf ₂ COSe	6	0.20	2.22	0.92	0.27
TiZrCO ₂	-3	1.19	0.07	-0.73	0.76	ZrHfCO ₂	-3	1.41	0.05	-0.23	0.47
	-1	1.41	0.05	-0.41	0.64		-1	1.63	0.04	0.12	0.32
	0	1.50	0.04	-0.27	0.58		0	1.72	0.03	0.29	0.24
	1	1.59	0.02	-0.14	0.52		1	1.80	0.03	0.43	0.17
TiHfCO ₂	-3	1.15	0.00	-0.73	0.65	3	1.94	0.02	0.69	0.03	
	-1	1.35	0.00	-0.42	0.54	5	2.04	0.01	0.91	-0.09	
	0	1.47	0.00	-0.28	0.52						
	1	1.53	0.00	-0.16	0.46						

sitions of these nine semiconducting MXenes at different strains. In each case, the alignments of band edges are shown only for the set of α for which the compound is semiconducting. For Sc₂COT MXenes, both VBM and CBM move to higher energies as strain changes from compressive to tensile. The decrease in E_g with α in the tensile region is mostly due to a gradual decrease in the change in the position of CBM. For Sc₂COSe in particular, larger changes in E_g in the compressive region are due to larger changes in the position of the CBM. For other compounds, though both bands move towards higher energies as strain increases from compressive to tensile, the changes in the positions of CBM are about 3 times larger than that of VBM. This explains the trends of E_g shown in Table I. In Reference [42], it was shown that a substantial electric field acts across the surfaces in M₂COT MXenes, resulting in a sizeable amount of band bending and subsequent re-alignment of VBM and CBM. The resulting potential difference $\Delta\Phi$ between the surfaces lifted the restriction on E_g as the band gap is now

modified to $(1.23 - \Delta\Phi)$ eV. As a consequence, Zr₂COS, Hf₂COS(Sc₂COS) turned out to be potential photocatalysts active in the IR(visible)-region. $\Delta\Phi$ between the two surfaces of M₂COT MXenes are presented in Table I. The potential profiles of the compounds are shown in Figure S6, supplementary information. We find that for all compounds, $\Delta\Phi$ increases monotonically with α from compressive to tensile region. The substantial values of $\Delta\Phi$ effect band straddling in Sc₂COS under compressive strain. Consequently, Sc₂COS can be considered as a photocatalyst where both OER and HER can take place simultaneously for the entire range of strains considered. In Sc₂COSe, $\Delta\Phi$ and the subsequent electric field are not enough to push the VBM below the OER potential. As a result, Sc₂COSe continues to be a catalyst for HER only. Compressive strain in IR-active Zr₂COS and Hf₂COS reduce $\Delta\Phi$ significantly destroying the alignment of CBM. Both HER and OER can continue to happen in these two compounds only for tensile strain. A large $\Delta\Phi$ in Hf₂COSe under 6% tensile strain

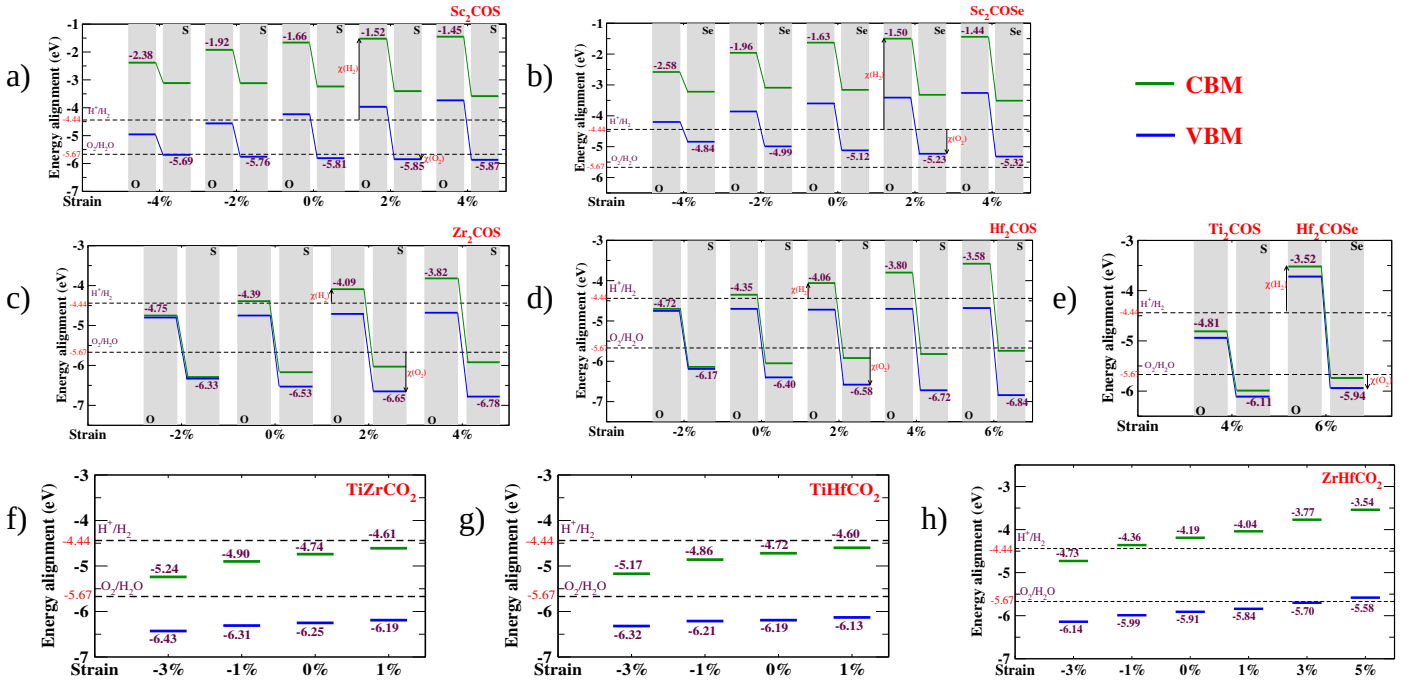


FIG. 2: Variations in the Band Edge Positions of a) Sc_2COS , b) Sc_2COSe , c) Zr_2COS d) Hf_2COS , f) TiZrCO_2 , g) TiHfCO_2 & h) ZrHfCO_2 with strain α . e) shows the Band Edge Positions of Ti_2COS at 4% & Hf_2COSe at 6% tensile strain. The Overpotentials for M_2COT MXenes are marked with arrows. The redox (HER and OER) potentials are marked by a dotted black line. Vacuum levels of the both surfaces are shifted to 0 eV.

generates a large electric field re-aligning the CBM and VBM at positions suitable for OER happening at the Se surface and HER at the O surface. In Ti_2COS at 4% tensile strain, $\Delta\Phi$ nearly half that of Hf_2COSe turns out to be not enough to push the CBM above that of HER potential. Consequently, Ti_2COS cannot be considered as a photocatalyst for water splitting even with finite strain. Application of strain fails to induce band straddling in TiZrCO_2 and TiHfCO_2 . A near-zero internal electric field is not enough to supply the necessary energy to push the CBM at energies above HER energy. In ZrHfCO_2 , the appropriate band alignments at zero strain are destroyed when α varies outside the range of [-1% : 3%]. Thus, only Sc_2COS , Zr_2COS , Hf_2COS , Hf_2COSe , ZrHfCO_2 for a range of strains can be considered for assessment of other parameters associated with photocatalytic efficiencies. It is worth noting that the overpotential $\chi(H_2)$ that is calculated as the difference between the CBM and HER energy has improved significantly upon application of tensile strain in Zr_2COS and Hf_2COS , a 0.57eV and 0.55eV jump for the former with a 4% change in α . For the later, the change is 0.77 eV when α changes by 6%. For Sc_2COS , overpotential $\chi(O_2)$, calculated as the difference between the

VBM and the OER energy, improves marginally while it degrades considerably in ZrHfCO_2 as α increases in the tensile region. For the new compound Hf_2COSe at 6% tensile strain, both overpotentials are substantial.

C. Optical Properties

In order for good STH efficiency, a photocatalyst should have high absorption ability in the infrared and visible part of the solar spectrum. This can be assessed by analysis of complex frequency-dependent dielectric function $\varepsilon(\omega) = \varepsilon_r(\omega) + i\varepsilon_{im}(\omega)$. The imaginary part of the dielectric function (ε_{im}) is obtained by summing over the empty states [51]:

$$\varepsilon_{\alpha\beta}^{im}(\omega) = \frac{4\pi^2 e^2}{\Omega} \lim_{q \rightarrow 0} \frac{1}{q^2} \sum_{c,v,k} 2\omega_k \delta(\varepsilon_{ck} - \varepsilon_{vk} - \omega) \times \langle u_{ck+e\alpha q} | u_{vk} \rangle \langle u_{vk} | u_{ck+e\beta q} \rangle$$

e is the electronic charge, Ω is the volume of the supercell, c and v denote the conduction and valance band states, respectively, ω is the frequency of the incident light. u_{ck} is the cell-periodic part of the orbitals at the point \mathbf{k} . The excitation is represented in terms of Dirac

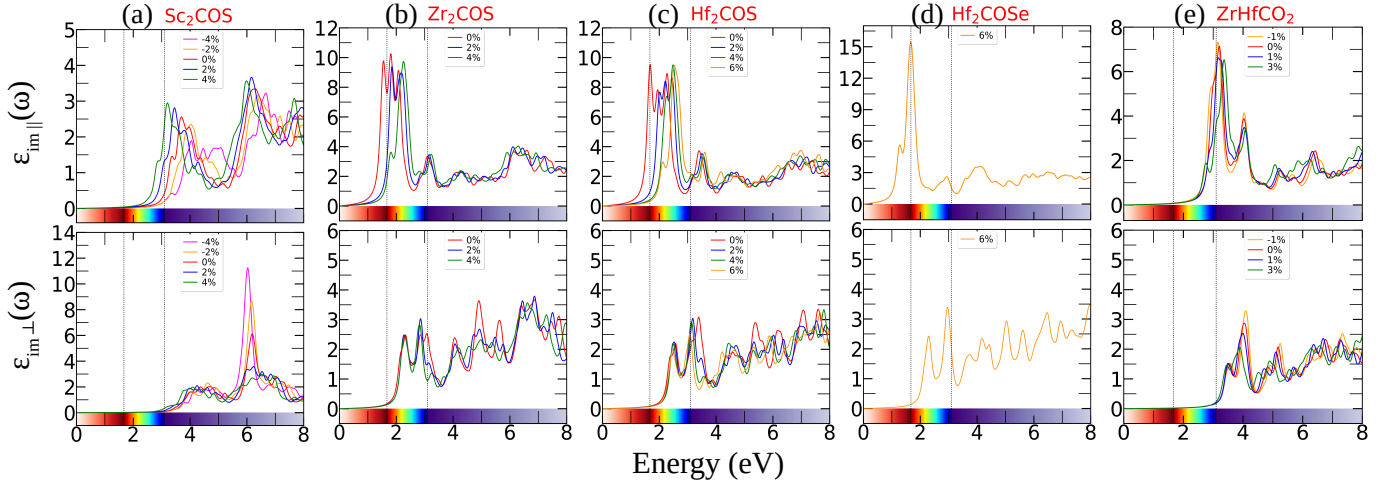


FIG. 3: Variations in the Imaginary Part of Dielectric Functions of a) Sc_2COS , b) Zr_2COS , c) Hf_2COS , d) Hf_2COSe and e) ZrHfCO_2 with biaxial strain α . The visible regions are marked by two black dotted lines. The \parallel and \perp symbols express the in-plane and out-of-plane directions, respectively.

δ . The real part of the dielectric function can be calculated using the Kramers-Kronig transformation :

$$\varepsilon_{\alpha\beta}^r(\omega) = 1 + \frac{2}{\pi} P \int_0^{\infty} \frac{\varepsilon_{\alpha\beta}^{im}(\omega')\omega'}{\omega'^2 - \omega^2 + i\eta} d\omega' \quad (1)$$

P stands for the Cauchy principal value of the integral, and η is the infinitesimal shift in the complex plane. Using ε_{im} & ε_r , the absorption coefficient $A(\omega)$ can be calculated as [52]:

$$A(\omega) = \frac{\sqrt{2}\omega}{c} \left\{ [\varepsilon_r^2(\omega) + \varepsilon_{im}^2(\omega)]^{1/2} - \varepsilon_r(\omega) \right\}^{1/2} \quad (2)$$

The imaginary part of the dielectric function denotes the absorption of solar energy during the transfer of electrons from VBM to CBM. In Figure 3, we present the in-plane and out-of-plane components of $\varepsilon_{im}(\omega)$ of the five Janus MXenes with variation of strain. Due to the strong anisotropy in the Janus MXenes, the in-plane ($\varepsilon_{im\parallel}$) and out-of-plane ($\varepsilon_{im\perp}$) components are quite different. The out-of-plane absorptions in each system happen mainly in the UV part of the solar spectrum. This implies that to get high absorption efficiency in the IR region, the MXene sheets should be held parallel to the light source.

Upon inspecting the in-plane component $\varepsilon_{im\parallel}$ of Sc_2COS , we find that in the absence of strain, there are two strong absorption peaks at 3.69 eV and 6.3 eV, both in the UV-region. In the tensile-strain regime, there is a red shift of the absorption spectra due to a gradual decrease in the band gap with an increase in strain. At $\alpha = 4\%$, the peak at 3.69 eV shifts to 3.2 eV. An exact opposite trend (blue shift) is observed in the case

of out-of-plane component $\varepsilon_{im\perp}$. Variations in the $\varepsilon_{im\parallel}$ of Zr_2COS and Hf_2COS with strain have similar characteristics. With no strain, both compounds show the strongest absorption in the IR region. The absorption spectra of Zr_2COS are characterised by a strong peak at 1.55 eV in the IR region followed by two peaks at 1.81 eV and 2.08 eV, both in the visible region. Here, too, the increase in tensile strain blue shifts the absorption spectra. This implies that zero or low tensile strain in these two compounds would enable them to tap the maximum part of the solar spectrum. The highest absorption in the IR region is observed in the case of Hf_2COSe under 6% tensile strain. The absorption spectra are characterised by a single strong peak at 1.67 eV (Fig. 3d). Since ZrHfCO_2 is predicted to be a visible-active photocatalyst, it is expected that it will absorb mostly from the visible part of the solar energy. In Figure 3(e), we find that its absorption spectra at zero strain are characterised by a strong peak at around 3.2 eV followed by smaller peaks at higher energy. Application of strain does not induce any significant shift of the spectrum suggesting that its absorption is completely in the visible and UV part of the solar spectrum. The results indicate that strained Hf_2COSe , Hf_2COS , and Zr_2COS under zero or small tensile strain can be photocatalysts with good STH conversion efficiency as their absorptions in the IR region are significant. Sc_2COS and ZrHfCO_2 will have STH efficiencies lower than these three as they absorb mostly visible and UV solar light.

TABLE II: Variations in the Energy Conversion Efficiency and Quantum Efficiency of Total (η_{abs} , η_{abs}^Q), Ultraviolet (η_{UV} , η_{UV}^Q), Visible (η_{VIS} , η_{VIS}^Q) and Infrared (η_{IR} , η_{IR}^Q) light absorption, Carrier Utilisation (η_{cu} , η_{cu}^Q), Solar-to-Hydrogen (η_{STH} , η_T^Q), Corrected Solar to Hydrogen (η'_{STH}), with Biaxial strain α for the five Janus compounds.

Compounds	α (%)	Energy Conversion Efficiencies							Quantum Efficiencies					
		η_{abs} (%)	η_{cu} (%)	η_{STH} (%)	η'_{STH} (%)	η_{UV} (%)	η_{VIS} (%)	η_{IR} (%)	η_{abs}^Q (%)	η_{cu}^Q (%)	η_T^Q (%)	η_{UV}^Q (%)	η_{VIS}^Q (%)	η_{IR}^Q (%)
Sc ₂ COS	-4	13.75	7.86	1.08	1.05	31.03	0.00	0.00	6.66	18.65	1.24	85.42	0.00	0.00
	-2	11.80	9.17	1.08	1.03	31.03	0.00	0.00	5.60	22.19	1.24	85.42	0.00	0.00
	0	13.75	11.78	1.62	1.51	36.32	0.70	0.00	6.66	27.96	1.86	100.00	1.22	0.00
	2	17.52	15.28	2.68	2.40	36.32	2.90	0.00	8.78	35.02	3.07	100.00	5.08	0.00
	4	22.87	19.26	4.41	3.73	36.32	6.51	0.00	11.99	42.21	5.06	100.00	11.39	0.00
Zr ₂ COS	0	99.44	84.21	83.74	37.55	36.32	57.14	100.00	97.63	98.50	96.17	100.00	100.00	94.28
	2	95.68	80.01	76.55	34.68	36.32	57.14	98.69	87.92	100.00	87.92	100.00	100.00	81.97
	4	88.21	73.20	64.57	30.71	36.32	57.14	73.96	74.15	100.00	74.15	100.00	100.00	61.43
Hf ₂ COS	0	99.56	84.41	84.04	38.54	36.32	57.14	100.00	98.12	98.37	96.52	100.00	100.00	94.80
	2	95.59	79.91	76.39	35.44	36.32	57.14	98.36	87.73	100.00	87.73	100.00	100.00	81.69
	4	88.11	73.12	64.43	31.30	36.32	57.14	73.68	73.99	100.00	73.99	100.00	100.00	61.19
	6	79.79	67.99	54.26	27.78	36.32	57.14	52.68	62.31	100.00	62.31	100.00	100.00	43.75
Hf ₂ COSe	6	100.00	76.40	76.40	29.71	36.32	57.14	98.37	99.99	87.75	87.74	100.00	100.00	81.70
ZrHfCO ₂	-1	52.40	30.77	16.13	15.97	36.32	30.95	0.00	33.73	54.91	18.52	100.00	54.17	0.00
	0	47.83	31.04	14.85	14.75	36.32	28.29	0.00	29.88	57.07	17.05	100.00	49.51	0.00
	1	43.81	26.10	11.43	11.37	36.32	21.16	0.00	26.65	49.27	13.13	100.00	37.04	0.00
	3	36.91	17.90	6.61	6.59	36.32	11.10	0.00	21.44	35.40	7.59	100.00	19.42	0.00

D. Solar Energy Conversion Efficiency

The real assessment of the utility of a photocatalyst for water splitting is incomplete unless its solar energy conversion efficiency is quantified. The relevant parameters are light absorption efficiency, carrier utilisation efficiency, and STH efficiency. Assuming 100% efficiency of the catalytic reactions, the efficiency of light absorption is defined as [5]

$$\eta_{abs} = \frac{\int_{E_g}^{\infty} P(\hbar\omega)d(\hbar\omega)}{\int_0^{\infty} P(\hbar\omega)d(\hbar\omega)} \quad (3)$$

$P(\hbar\omega)$ denotes the incident AM1.5G solar flux at photon energy $\hbar\omega$, and E_g is the band gap of materials. The quantity in the numerator is the power density absorbed by the catalyst while the one in the denominator stands for the incident power density of sunlight (AM 1.5G), implying that η_{abs} is the ratio of converted energy to the total energy. A related quantity is the quantum efficiency of the catalyst, defined as the ratio of the number

of utilised photons to the total number of incident photons,

$$\eta_{abs}^Q = \frac{\int_{E_g}^{\infty} \frac{P(\hbar\omega)}{\hbar\omega} d(\hbar\omega)}{\int_0^{\infty} \frac{P(\hbar\omega)}{\hbar\omega} d(\hbar\omega)} \quad (4)$$

The carrier utilisation efficiency is defined as

$$\eta_{cu} = \frac{\Delta G \int_E^{\infty} \frac{P(\hbar\omega)}{\hbar\omega} d(\hbar\omega)}{\int_{E_g}^{\infty} P(\hbar\omega)d(\hbar\omega)} \quad (5)$$

The related quantity, quantum efficiency of carrier utilisation is given by [5]

$$\eta_{cu}^Q = \frac{\int_E^{\infty} \frac{P(\hbar\omega)}{\hbar\omega} d(\hbar\omega)}{\int_{E_g}^{\infty} \frac{P(\hbar\omega)}{\hbar\omega} d(\hbar\omega)} \quad (6)$$

$\Delta G = 1.23$ eV is the energy difference between redox potential $\text{H}_2\text{O}/\text{O}_2$ and H^+/H_2 . The calculation of efficiency crucially depends on the extra energy required

to overcome the barriers of HER and OER, which can be quite large. Co-catalysts are often used to circumvent this difficulty in experiments. In previous experiments, it was reported that the overpotentials of IrO_x , NiFeO_x , NiCoO_x , and CoFeO_x co-catalysts for OER are below 0.5 eV [53] and that of Pt co-catalysts for HER is lower than 0.1 eV [54]. Therefore, considering energy loss due to carrier migration between two surfaces of the catalyst, we assume an overpotential of 0.6 eV (0.2 eV) for OER(HER). Practically, the photons which have energy greater than E are utilised in water-splitting reactions while the materials absorb energy greater than E_g . Then, E is determined as follows.

$$\begin{aligned}
E &= E_g; \chi(H_2) \geq 0.2eV, \chi(O_2) \geq 0.6eV \\
&= E_g + 0.6 - \chi(O_2); \chi(H_2) \geq 0.2eV, \chi(O_2) < 0.6eV \\
&= E_g + 0.2 - \chi(H_2); \chi(H_2) < 0.2eV, \chi(O_2) \geq 0.6eV \\
&= E_g + 0.8 - \chi(H_2) - \chi(O_2); \chi(H_2) < 0.2eV, \\
&\quad \chi(O_2) < 0.6eV
\end{aligned} \tag{7}$$

Clearly, large $\chi(H_2)$ and $\chi(O_2)$ lead to greater η_{cu} as the energy window of photon absorption increases. Using the full solar spectrum, the Solar-to-Hydrogen conversion efficiency and associated quantum efficiency are calculated as [5]:

$$\eta_{STH} = \eta_{abs} \times \eta_{cu} \tag{8}$$

$$\eta_T^Q = \eta_{abs}^Q \times \eta_{cu}^Q \tag{9}$$

The intrinsic electric fields across the surfaces in M_2COT compounds help in the separation of electron-hole pairs. The work done by this field is, therefore, to be taken into account. The STH efficiency (η'_{STH}), after taking this into consideration is [5]:

$$\eta'_{STH} = \frac{\Delta G \int_E^\infty \frac{P(\hbar\omega)}{\hbar\omega} d(\hbar\omega)}{\int_0^\infty P(\hbar\omega) d(\hbar\omega) + \Delta\Phi \int_{E_g}^\infty \frac{P(\hbar\omega)}{\hbar\omega} d(\hbar\omega)} \tag{10}$$

where $\Delta\Phi$ is the potential difference between two surfaces of Janus Mxene.

In Table II, we present these parameters calculated at various α for the five Janus compounds. Additionally, we present results of quantum ($\eta_{UV}^Q, \eta_{VIS}^Q, \eta_{IR}^Q$) and energy conversion efficiencies ($\eta_{UV}, \eta_{VIS}, \eta_{IR}$) of UV, visible and IR lights. The range of IR, Visible, and UV light considered for calculating these are < 1.65 eV, 1.65-3.10 eV, and > 3.10 eV, respectively. We find that the maximum corrected STH efficiency η'_{STH} obtained in the cases of unstrained Zr_2COS and Hf_2COS far exceeds the

maximum obtained efficiency in a number of 2D photocatalysts. The maximum efficiency in MoSSe is $\sim 15\%$ [16], in WSSe $\sim 8\%$ - 16% [18], in SiPN $\sim 8.37\%$, in SiAsP $\sim 11\%$, in SiSbP $\sim 20\%$, in SiSbAs $\sim 13\%$ [21], in Janus PtSO $\sim 7.62\%$, in PtSeO $\sim 23\%$ [19], in Janus $\text{In}_2\text{X}_2\text{X}'$ (X and X' = S, Se, and Te) $\sim 10\%$ - 21% [55] and in M_2X_3 $\sim 20\%$ - 32% [5], way lower than $\sim 30\%$ - 39% obtained in the IR-active systems considered in this work. Among the two visible-active systems, Sc_2COS has a maximum STH efficiency of $\sim 4\%$ while it is $\sim 16\%$ for ZrHfCO_2 . This significant dissimilarity in η'_{STH} of IR-active and visible-active compounds is due to huge differences in energy conversion as well as carrier utilisation efficiencies.

The origin of such differences can be understood from energy conversion and carrier utilisation efficiencies associated with different parts of the solar spectrum. A look at the quantum efficiencies reveals that the three IR-active MXenes have 100% UV and visible light absorption efficiencies while it varies between 44-95 % for IR light. The carrier utilisation efficiency is between 88-100%. In contrast, the visible-active MXenes have no efficiency in the absorption of IR light. Even the efficiencies are only about 55% (for ZrHfCO_2) for visible light. In Sc_2COS , it is remarkably poor ($\sim 1\%$ - 11%). The carrier utilisation efficiencies vary between 19-42 % in Sc_2COS and between 35-55 % in ZrHfCO_2 . The large band gaps in these two compounds lead to absorption of only 6-12 % of photons for Sc_2COS while it is 21-33 % for ZrHfCO_2 . In comparison, 62-100 % of photons are absorbed by the IR-active compounds. Strained Hf_2COSe , the one with the best absorbance in the IR region, absorbs almost 100 % photons. But its carrier utilisation efficiency is only about 88%, not as great as the other two IR-active MXenes. The energy conversion efficiency of this compound, however, is about $\sim 30\%$, close to Zr_2COS and Hf_2COS at 4% strain.

The overpotentials that are very important in shaping the efficiency parameters of a photocatalyst can be understood from their variations with strain. Hf_2COSe having the smallest band gap of 0.2 eV (Table I) has the largest η_{abs} but its η_{cu} is less than that of Zr_2COS and Hf_2COS when the later two are subjected to a tensile strain upto 2%. The origin of this lies in the value of E , the minimum energy of photons practically used for water splitting, and the size of the band gap (Equation (7)). Though Hf_2COSe has large $\chi(H_2)$, only 0.27 eV $\chi(O_2)$ implies $E = 0.53$ eV, higher than 0.51(0.47) eV for Zr_2COS (Hf_2COS) at 0 % strain. At 2% strain, although

TABLE III: Carrier Effective Mass (m_i^*), In Plane Stiffness Constants (C_i), Deformation Potentials (E_i) and Carrier Mobilities (μ_i) of electrons and holes along x and y directions of Janus MXenes at their equilibrium volumes. The Carrier Effective Masses are presented in the unit of electron mass $m_0=9.11\times 10^{-31}$ kg.

Compounds	Carrier	m_x^*	m_y^*	C_x	C_y	E_x	E_y	μ_x	μ_y
	Type	(m_0)	(m_0)	(Nm^{-1})	(Nm^{-1})	(eV)	(eV)	($\text{cm}^2\text{V}^{-1}\text{s}^{-1}$)	($\text{cm}^2\text{V}^{-1}\text{s}^{-1}$)
Sc ₂ COS	e ⁻	0.935	0.965	123.965	123.783	3.76	3.74	142.91	135.40
	h ⁺	0.829	0.551			1.43	1.33	1256.81	3284.03
Zr ₂ COS	e ⁻	2.232	0.161	212.210	212.060	3.88	2.58	40.31	17511.38
	h ⁺	0.194	0.194			4.29	4.82	4365.16	3455.52
Hf ₂ COS	e ⁻	1.887	0.147	234.772	234.495	3.30	2.86	46.26	18902.51
	h ⁺	0.392	0.182			5.19	5.30	808.15	3590.80
Hf ₂ COSe 6%	e ⁻	3.197	0.173	142.741	135.349	2.82	2.61	25.02	9458.77
	h ⁺	0.325	0.160			7.32	7.81	359.35	1235.00
ZrHfCO ₂	e ⁻	2.044	0.275	278.055	277.925	7.98	8.13	14.89	792.20
	h ⁺	0.215	0.215			3.54	3.13	6839.12	8744.08

Zr₂COS(Hf₂COS) is 0.63eV(0.66eV) greater than that of Hf₂COSe, the much smaller E_g of Hf₂COSe makes the denominator in Equation (5) dominating, resulting in lower η_{cu} of it compared to that of Zr₂COS and Hf₂COS. Substantial increase in their $\chi(H_2)$ and E_g as tensile strain goes beyond 2% implies Zr₂COS(Hf₂COS) can use photons with energy 0.86(0.9) eV and above. This reduces their η_{cu} at higher strain. The variations in η_{abs} and η_{cu} with strain in Sc₂COS and ZrHfCO₂ can be explained in a similar way.

E. Carrier Mobility

Carrier mobility is another crucial parameter in deciding the efficiency of a photocatalyst. In this work, we obtain the carrier mobility using the Deformation Potential (DP) theory [56]. In this theory, carrier mobility is determined primarily by the interactions of electrons and acoustic phonons. The carrier mobility along direction i is calculated using the expression

$$\mu_i = \frac{2e\hbar^3 C_i}{3k_B T |m_i^*|^2 E_i^2} \quad (11)$$

Here, e , k_B , and T represent the electronic charge, Boltzmann constant, and temperature, respectively. $m_i^* = \hbar^2 \left[\frac{\partial^2 E_k}{\partial k^2} \right]^{-1/2}$ is the carrier effective mass derived from fitting the band edges where E_k is the band energy corresponding to wave vector k . $E_i = \left(\frac{\partial E_{edge}}{\partial \delta_i} \right)$ is the De-

formation Potential that denotes the shift of band edges E_{edge} (CBM/VBM) under uniaxial strain δ_i along direction i . The in-plane stiffness constant along direction i is determined by $C_i = \frac{1}{S_0} \left(\frac{\partial^2 E_{total}}{\partial \delta_i^2} \right)$ where E_{total} is the total energy of the system and S_0 is the surface area of the equilibrium volume. C_i and E_i are obtained by varying δ_i from -2% to 2% along x and y directions and fitting the corresponding changes in E_{total} and E_{edge} to appropriate functions. Calculated values of stiffness constants (C_i), effective masses (m_i^*), deformation potentials (E_i), and mobilities (μ_i) of each carrier type are shown in Table III. The results are for systems without strain except for Hf₂COSe, where the system under 6% tensile strain is considered.

The results clearly show qualitative differences between carrier mobilities of IR-active and visible-active systems. For visible-active Sc₂COS and ZrHfCO₂, electron mobility, irrespective of direction, is the order of magnitude less than the hole mobility. For IR-active Zr₂COS, Hf₂COS, and Hf₂COSe, the relative strengths of carrier mobility is direction dependent: holes(electrons) have an order of magnitude greater mobility along $x(y)$ -direction. However, the common feature in all of them is the significant difference in electron and hole carrier mobilities. Larger effective mass and deformation potential of electrons are responsible for significant small electron mobility in Sc₂COS and ZrHfCO₂. These, in turn, occur due to the relatively flat CBM of these compounds. In the three IR-active MXenes, the

electron and hole effective masses along y are nearly the same. Along x -direction, electron effective masses are the order of magnitude larger. This explains why hole mobility along x is orders of magnitude larger in these compounds. On the other hand, the reason behind the order of magnitude larger electron mobility with respect to that of holes along y is driven by the larger deformation potential of holes with respect to that of electrons.

The separation of carriers with opposite polarity enhances, resulting in less probability of carrier recombination if mobilities of different carriers have different preferential directions. For visible-active $\text{Sc}_2\text{COS}(\text{ZrHfCO}_2)$, electrons(holes) have no preferential direction for migration while holes(electrons) have greater mobility along y . Among the three IR-active photocatalysts, both carriers in Hf_2COT ($T = \text{S}, \text{Se}$) have greater preference along y . Different carriers in Zr_2COS have different preferential directions for migration. While it is y for electrons, holes have greater preference along x . Thus, for all five compounds, good carrier separation leading to less probability of carrier recombination is prominent.

Upon comparing the carrier mobilities of well known 2D photocatalysts ($270 \text{ cm}^2\text{V}^{-1}\text{s}^{-1}$, $130 \text{ cm}^2\text{V}^{-1}\text{s}^{-1}$ for MoS_2 , $90 \text{ cm}^2\text{V}^{-1}\text{s}^{-1}$, $25 \text{ cm}^2\text{V}^{-1}\text{s}^{-1}$ for MoSe_2 , $540 \text{ cm}^2\text{V}^{-1}\text{s}^{-1}$, $320 \text{ cm}^2\text{V}^{-1}\text{s}^{-1}$ for WS_2 , $270 \text{ cm}^2\text{V}^{-1}\text{s}^{-1}$, $30 \text{ cm}^2\text{V}^{-1}\text{s}^{-1}$ for WSe_2 [57], $210 \text{ cm}^2\text{V}^{-1}\text{s}^{-1}$, $53 \text{ cm}^2\text{V}^{-1}\text{s}^{-1}$ for MoSSe [16], $723 \text{ cm}^2\text{V}^{-1}\text{s}^{-1}$, $125 \text{ cm}^2\text{V}^{-1}\text{s}^{-1}$ for WSSe [18]) we find that carrier mobilities in Janus compounds considered here are far better. However, a comparison of mobilities among these Janus and their endpoint compounds M_2CO_2 produces mixed results. Mobilities of Hf_2COT are far greater than Hf_2CO_2 where $\mu^h \sim 1.6$ to $2.2 \times 10^3 \text{ cm}^2\text{V}^{-1}\text{s}^{-1}$, $\mu^e \sim 0.12$ to $2.2 \times 10^3 \text{ cm}^2\text{V}^{-1}\text{s}^{-1}$ [33]. Same happens upon comparison between Zr_2COS and Zr_2CO_2 . The later has hole(electron) mobilities of $2.3 \times 10^3 \text{ cm}^2\text{V}^{-1}\text{s}^{-1}$ and $1.7 \times 10^3 \text{ cm}^2\text{V}^{-1}\text{s}^{-1}$ ($83 \text{ cm}^2\text{V}^{-1}\text{s}^{-1}$ and $1.1 \times 10^3 \text{ cm}^2\text{V}^{-1}\text{s}^{-1}$) along two directions. In case of ZrHfCO_2 , the hole(electron) mobilities are higher(lower) than end point compounds Zr_2CO_2 and Hf_2CO_2 while the mobilities of both carriers in Sc_2COS are significantly lower than the conventional counterpart Sc_2CO_2 ($\mu^h \sim 6.4$ to $9.5 \times 10^3 \text{ cm}^2\text{V}^{-1}\text{s}^{-1}$, $\mu^e \sim 6.1$ to $12.5 \times 10^3 \text{ cm}^2\text{V}^{-1}\text{s}^{-1}$ [58]).

F. Exciton Binding Energy

The Coulomb interaction between the photo-excited electron and hole pairs is attractive, resulting in exciton-bound states. The exciton binding energy representing the strength of this interaction directly affects the photocatalytic efficiency. Excitons can transfer momentum and energy but no charge to the radicals, reducing the efficiency of the water-splitting process. In 2D materials, the reduced dielectric screening enhances the exciton binding energy. A first-principles-based investigation in this regard requires the coupling of many-body perturbation theory to the Bethe-Salpeter equation. This approach is computationally expensive. The difficulty can be circumvented by adopting a 2D hydrogenic exciton model for an anisotropic system within the Keldysh formalism [59–61]. Several comparisons with the many-body perturbation theory-based GW-BSE method have demonstrated the accuracy of this model[13, 62, 63]. Therefore, in this work, we have used this model to calculate the exciton binding energies of the Janus MXenes. In this model, the Hamiltonian for the excitons is

$$H = -\frac{\hbar^2}{2} \left(\frac{1}{\mu_{rx}} \frac{\partial^2}{\partial x^2} + \frac{1}{\mu_{ry}} \frac{\partial^2}{\partial y^2} \right) + V_{2D}(x, y) \quad (12)$$

Here, μ_{rx} & μ_{ry} are the reduced masses of the excitons along x and y directions and can be derived by the following relation: $\mu_{ri} = (m_{ei}^{*-1} + m_{hi}^{*-1})$, $i = x, y$. m_{ei}, m_{hi} are the effective mass of electrons and holes along i , respectively. The Coulomb potential between electron and hole in a 2D dielectric substrate can be represented as

$$V_{2D}(r) = -\frac{e^2}{4(\varepsilon_1 + \varepsilon_2)\varepsilon_0 r_0} \left[H_0 \left(\frac{r}{r_0} \right) - Y_0 \left(\frac{r}{r_0} \right) \right] \quad (13)$$

Here, H_0 and Y_0 are the zeroth order Struve and Bessel functions, respectively. $\varepsilon_{1,2}$ are the dielectric constants of the two mediums (both vacuum in our case), and ε_0 denotes the vacuum permittivity. r_0 , the screening length is evaluated using 2D polarizability χ_{2D} : $r_0 = \left(\frac{4\pi}{\varepsilon_1 + \varepsilon_2} \right) \chi_{2D}$. χ_{2D} is related to the static dielectric constant $\varepsilon(0)$ of the 2D material: $\varepsilon(0) = \left(1 + \frac{4\pi\chi_{2D}}{L} \right)$, L is the size of the vacuum between two mono-layers (20 \AA in our case). For $r > r_0$, the potential behaves like a simple Coulomb potential while for $r < r_0$, it diverges logarithmically and can be expressed

TABLE IV: Variations in the Carrier Effective Mass ($m_{ex}^*, m_{hx}^*, m_{ey}^*, m_{hy}^*$), Reduced Mass (μ_{rx}, μ_{ry}) along x and y directions, Static Dielectric Constant ($\varepsilon(0)$), 2D Polarisability (χ_{2D}), theoretically predicted and numerically calculated Exciton Extensions (λ_{th}, λ), Exciton Bohr radii (a_x, a_y) and Exciton Binding Energy (E_b) of Janus MXenes with Biaxial strain (α), calculated using the Hydrogenic Exciton model.

Compounds	α (%)	m_{ex}^* (m_0)	m_{hx}^* (m_0)	μ_{rx} (m_0)	m_{ey}^* (m_0)	m_{hy}^* (m_0)	μ_{ry} (m_0)	$\varepsilon(0)$	χ_{2D} (\AA)	λ_{th} $\sim (\frac{\mu_{rx}}{\mu_{ry}})^{1/3}$	λ	a_x (\AA)	a_y (\AA)	E_b (eV)
Sc ₂ COS	-4	1.172	0.813	0.48	1.168	0.553	0.38	2.65	2.63	1.09	1.09	4.82	5.24	1.23
	-2	0.988	0.819	0.45	1.003	0.558	0.36	2.67	2.65	1.08	1.08	5.01	5.41	1.21
	0	0.935	0.829	0.44	0.965	0.551	0.35	2.70	2.71	1.08	1.08	5.11	5.52	1.18
	2	0.948	0.833	0.44	0.997	0.542	0.35	2.75	2.78	1.08	1.08	5.15	5.58	1.16
	4	0.985	0.838	0.45	1.065	0.529	0.35	2.80	2.87	1.09	1.09	5.17	5.63	1.14
Zr ₂ COS	0	2.232	0.194	0.18	0.161	0.194	0.09	6.47	8.70	1.27	1.28	14.97	19.09	0.37
	2	2.592	0.361	0.32	0.191	0.361	0.12	5.57	7.27	1.36	1.38	10.35	14.24	0.48
	4	3.196	0.358	0.32	0.223	0.358	0.14	5.17	6.64	1.33	1.34	9.76	13.06	0.52
Hf ₂ COS	0	1.887	0.392	0.32	0.147	0.182	0.08	5.93	7.85	1.59	1.61	11.17	17.95	0.42
	2	2.061	0.385	0.32	0.170	0.184	0.09	5.12	6.56	1.54	1.56	10.19	15.94	0.48
	4	2.306	0.380	0.33	0.193	0.185	0.09	4.75	5.97	1.51	1.53	9.66	14.80	0.52
	6	2.656	0.375	0.33	0.218	0.190	0.10	4.56	5.67	1.48	1.50	9.33	13.97	0.55
Hf ₂ COSe	6	3.197	0.325	0.30	0.173	0.160	0.08	6.91	9.41	1.53	1.54	12.59	19.44	0.37
ZrHfCO ₂	-1	1.955	0.214	0.19	0.253	0.214	0.12	3.57	4.09	1.18	1.19	10.00	11.93	0.66
	0	2.044	0.215	0.19	0.275	0.215	0.12	3.51	4.00	1.17	1.18	9.83	11.59	0.67
	1	2.152	0.514	0.41	0.295	0.217	0.13	3.48	3.94	1.49	1.51	6.99	10.56	0.76
	3	2.419	0.498	0.41	0.348	0.217	0.13	3.45	3.89	1.46	1.47	6.90	10.18	0.78

as [60]:

$$V_{2D}^C(r) = -\frac{e^2}{4\pi\tilde{\varepsilon}\varepsilon_0 r_0} \left[\ln\left(\frac{r}{r+r_0}\right) + [\gamma - \ln(2)]e^{-\left(\frac{r}{r_0}\right)} \right] \quad (14)$$

$\gamma \approx 0.5772$ is the Euler constant and $\tilde{\varepsilon} = \frac{\varepsilon_1 + \varepsilon_2}{2}$.

Using the variational method, the exciton wave function for an anisotropic material like Janus MXenes can be written as :

$$\begin{aligned} \Psi(x, y) &= \sqrt{\frac{2}{\pi a_x a_y}} \exp \left[-\left\{ \left(\frac{x}{a_x}\right)^2 + \left(\frac{y}{a_y}\right)^2 \right\}^{1/2} \right] \\ &= \sqrt{\frac{2}{\pi \lambda a_x^2}} \exp \left[-\left\{ \left(\frac{x}{a_x}\right)^2 + \left(\frac{y}{\lambda a_x}\right)^2 \right\}^{1/2} \right] \end{aligned} \quad (15)$$

Here, $a_x, a_y = \lambda a_x$ are the excitonic radii along the x and y direction, and λ is the variational anisotropy scaling

factor. Using the above trial wave function, the variational exciton binding energy is obtained as

$$E_b^{2D}(a_x, \lambda) = E_{kin}^{2D}(a_x, \lambda) + E_{pot}^{2D}(a_x, \lambda). \quad (16)$$

where

$$\begin{aligned} E_{kin}^{2D}(a_x, \lambda) &= -\frac{\hbar^2}{2} \iint \Psi^* \left[\frac{1}{\mu_{rx}} \frac{\partial^2 \Psi}{\partial x^2} + \frac{1}{\mu_{ry}} \frac{\partial^2 \Psi}{\partial y^2} \right] dx dy \\ &= \frac{\hbar^2}{4a_x^2} \left[\frac{1}{\mu_{rx}} + \frac{1}{\lambda^2 \mu_{rx}} \right] \end{aligned} \quad (17)$$

and

$$E_{pot}^{2D}(a_x, \lambda) = \iint V_{2D}^C(x, y) |\Psi(x, y)|^2 dx dy \quad (18)$$

are the contributions from kinetic and potential energies, respectively. The equations(16)-(18) are solved numerically. $E_b^{2D}(a_x, \lambda)$ is minimised with respect to the variational parameters a_x and λ to obtain the actual binding energy E_b .

The computed values of the carrier effective masses (m_{ei}^*, m_{hi}^*), static Dielectric constant $\varepsilon(0)$, exciton radii

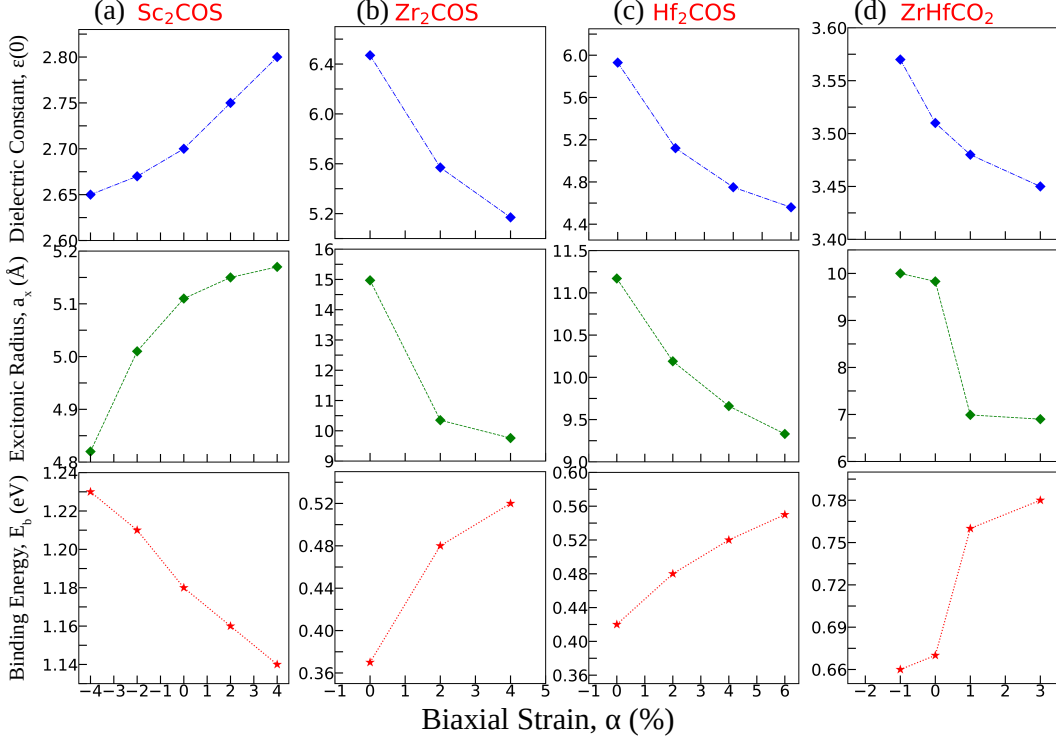


FIG. 4: Variations of Static Dielectric Constant $\epsilon(0)$, Exciton Radius (a_x) and Exciton Binding Energy (E_b) of a) Sc₂COS, b) Zr₂COS, c) Hf₂COS and d) ZrHfCO₂ with Biaxial strain (α).

(a_x , a_y), and exciton binding energy (E_b) of the five Janus MXenes with variation of strain α are presented in Table IV. Variations of the last three quantities with strain are also plotted in Figure 4. Comparison between numerically obtained (λ) and theoretically calculated ($\lambda_{th} \sim (\frac{\mu_{rx}}{\mu_{ry}})^{1/3}$ [59]) anisotropy parameter is also presented in Table IV. We find excellent agreement between these two for all systems and at all values of α . We find lower E_b for the IR-active photocatalysts in comparison to the visible-active ones with Sc₂COS producing the highest values.

The origin of the qualitative behavior of E_b across compounds and strain can be understood from the behavior of static dielectric constant and exciton radii. Larger $\epsilon(0)$ amounts to larger dielectric screening between electron-hole pairs. This is reflected in larger screening length r_0 and exciton radii a_i . From Table IV, we find that the static dielectric constant $\epsilon(0)$ is much larger in the three IR-active Janus MXenes in comparison with the visible-active ones. As a result, these systems have larger polarisability χ_{2D} . The screening length r_0 and exciton radii a_i are also larger as a consequence affecting lower E_b . Among the two visible-active

photocatalysts, lower $\epsilon(0)$ and χ_{2D} in Sc₂COS results in lower screening length, lower exciton radii and higher E_b as a consequence. With strain E_b decreases (increases) marginally in Sc₂COS (ZrHfCO₂) as a consequence of directions of variations in $\epsilon(0)$, χ_{2D} , r_0 and a_i . The same happens for IR-active Zr₂COS and Hf₂COS. With increasing strain, the opposite trends in Sc₂COS and the rest can be traced back to the variations in the electronic band gaps. With increasing strain, E_g decreases in Sc₂COS while it increases for the rest. The decrease in E_g leads to larger dielectric screening. In fact, the root of the qualitative trend of E_b across compounds can be explained this way.

The exciton binding energies of the Janus compounds considered in this work compare very well with those of well-known 2D photocatalysts. The range of E_b in our case, 0.37-1.23 eV, is in good agreement with MoS₂ ($E_b=1.03$ eV) [12], MoSe₂ ($E_b=0.91$ eV) [12], WS₂ ($E_b=1.04$ eV) [12], WSe₂ ($E_b=0.90$ eV) [12], WSSe ($E_b=0.83$ eV) [18], GeS ($E_b=0.98$ eV) [13], GeSe ($E_b=0.38$ eV) [13], GeTe ($E_b=0.21$ eV) [13], SnS ($E_b=0.50$ eV) [13] and SnSe ($E_b=0.28$ eV) [13].

IV. CONCLUSIONS

Extensive DFT-based calculations have been performed on 14 compounds from the family of M_2COT ($M=Sc, Ti, Zr, Hf$; $T=S, Se$) and $MM'CO_2$ ($M, M'=Sc, Ti, Zr, Hf$) Janus MXenes to find new photocatalysts for water splitting reactions, active in visible or IR part of the solar spectrum. The compounds have been chosen from a previous elaborate study [42] that predicted four new photocatalysts. Bi-axial strain, both compressive and tensile, have been applied on the compounds to either open an electronic band gap in semi-metals and/or to enforce alignments of band edges so that water-splitting reactions are possible. We found that the four existing Janus MXenes that had the proper band alignment to effect water splitting reactions preserved it when subjected to tensile strain up to 4%. In the course of the study, Hf_2COSe is found to be a new photocatalyst active in the IR region when subjected to 6% strain. We compute various performance parameters of these five compounds, varying the amount of tensile strain. We find that IR active Zr_2COS , Hf_2COS at equilibrium and low strain along with 6% strained Hf_2COSe have absorbance, carrier utilisation, carrier separation, exciton

binding, and solar-to-hydrogen conversion efficiency that are far superior than the well known 2D photocatalysts for water splitting reactions. Among the visible-active photocatalysts, Sc_2COS cannot meet the benchmark of 10% solar-to-hydrogen conversion efficiency while the performance parameters of $ZrHfCO_2$ are, at best, moderate. To our knowledge, this is the first comprehensive work demonstrating the utility of Janus MXenes as catalysts in photo-assisted water-splitting reactions. The work paves the way for further exploration into the family of MXenes to discover more photocatalysts for water-splitting reactions, a sustainable source of green energy.

ACKNOWLEDGEMENT

The authors gratefully acknowledge the Department of Science and Technology, India, for the computational facilities under Grant No. SR/FST/P-II/020/2009 and IIT Guwahati for the PARAM supercomputing facility where all computations are performed. The authors would like to thank Dr. Mukul Kabir for useful discussions.

-
- [1] C. R. Cox, J. Z. Lee, D. G. Nocera, and T. Buonassisi, *Proc. Natl. Acad. Sci.* **111**, 14057 (2014).
- [2] O. Khaselev, A. Bansal, and J. Turner, *Int. J. Hydrogen Energy* **26**, 127 (2001).
- [3] K. Maeda and K. Domen, *J. Phys. Chem. Lett.* **1**, 2655 (2010).
- [4] M. G. Walter, E. L. Warren, J. R. McKone, S. W. Boettcher, Q. Mi, E. A. Santori, and N. S. Lewis, *Chem. Rev.* **110**, 6446 (2010).
- [5] C.-F. Fu, J. Sun, Q. Luo, X. Li, W. Hu, and J. Yang, *Nano Lett.* **18**, 6312 (2018).
- [6] Y. Gai, J. Li, S.-S. Li, J.-B. Xia, and S.-H. Wei, *Phys. Rev. Lett.* **102**, 036402 (2009).
- [7] A. Kudo and Y. Miseki, *Chem. Soc. Rev.* **38**, 253 (2009).
- [8] C.-F. Fu, Q. Luo, X. Li, and J. Yang, *J. Mater. Chem. A* **4**, 18892 (2016).
- [9] J. Yang, D. Wang, H. Han, and C. Li, *Acc. Chem. Res.* **46**, 1900 (2013).
- [10] F. E. Osterloh, *Chem. Soc. Rev.* **42**, 2294 (2013).
- [11] X. Li, Z. Li, and J. Yang, *Phys. Rev. Lett.* **112**, 018301 (2014).
- [12] A. Ramasubramaniam, *Phys. Rev. B* **86**, 115409 (2012).
- [13] L. Xu, M. Yang, S. J. Wang, and Y. P. Feng, *Phys. Rev. B* **95**, 235434 (2017).
- [14] J. Wen, J. Xie, X. Chen, and X. Li, *Appl. Surf. Sci.* **391**, 72 (2017).
- [15] A.-Y. Lu, H. Zhu, J. Xiao, C.-P. Chuu, Y. Han, M.-H. Chiu, C.-C. Cheng, C.-W. Yang, K.-H. Wei, Y. Yang, *et al.*, *Nat. Nanotechnol.* **12**, 744 (2017).
- [16] L. Ju, M. Bie, J. Shang, X. Tang, and L. Kou, *JPhys Materials* **3**, 022004 (2020).
- [17] X. Ma, X. Wu, H. Wang, and Y. Wang, *J. Mater. Chem. A* **6**, 2295 (2018).
- [18] L. Ju, M. Bie, X. Tang, J. Shang, and L. Kou, *ACS Appl. Mater. Interfaces.* **12**, 29335 (2020).
- [19] H. Shen, Y. Zhang, G. Wang, W. Ji, X. Xue, and W. Zhang, *Phys. Chem. Chem. Phys.* **23**, 21825 (2021).
- [20] Y. Fan, X. Ma, J. Wang, X. Song, A. Wang, H. Liu, and M. Zhao, *Sci. Bull.* **65**, 27 (2020).
- [21] Y. Zhao, B. Zhang, and J. Lin, *Appl. Surf. Sci.* **621**, 156883 (2023).
- [22] R. Ma, Z. Chen, D. Zhao, X. Zhang, J. Zhuo, Y. Yin, X. Wang, G. Yang, and F. Yi, *J. Mater. Chem. A* **9**, 11501 (2021).

- [23] J. Zhou, X. Zha, F. Y. Chen, Q. Ye, P. Eklund, S. Du, and Q. Huang, *Angew. Chem. Int. Ed* **55**, 5008 (2016).
- [24] K. Luo, X.-H. Zha, Q. Huang, C.-T. Lin, M. Yang, S. Zhou, and S. Du, *RSC Adv.* **10**, 44430 (2020).
- [25] A. Mostafaei and M. Abbasnejad, *J. Alloys Compd.* **857**, 157982 (2021).
- [26] X.-H. Li, L. Shan-Shan, H.-L. Cui, and R.-Z. Zhang, *ACS Omega* **5**, 22248 (2020).
- [27] Q. He, H. Hu, Y. Shao, and Z. Zhao, *Optik* **247**, 167629 (2021).
- [28] Y. Zhang, N. Ma, Y. Wang, B. Liang, and J. Fan, *Appl. Surf. Sci.* **623**, 156827 (2023).
- [29] X. Yang, Z. Lu, C. Cheng, Y. Wang, X. Zhang, Z. Yang, and W. Lu, *J. Phys. Chem. C* **124**, 4090 (2020).
- [30] D. Kan, D. Wang, X. Zhang, R. Lian, J. Xu, G. Chen, and Y. Wei, *J. Mater. Chem. A* **8**, 3097 (2020).
- [31] W. Meng, X. Liu, H. Song, Y. Xie, X. Shi, M. Dargusch, Z.-G. Chen, Z. Tang, and S. Lu, *Nano Today* **40**, 101273 (2021).
- [32] H. Yu, Y. Wang, Y. Jing, J. Ma, C.-F. Du, and Q. Yan, *Small* **15**, 1901503 (2019).
- [33] Z. Guo, J. Zhou, L. Zhu, and Z. Sun, *J. Mater. Chem. A* **4**, 11446 (2016).
- [34] H. Zhang, G. Yang, X. Zuo, H. Tang, Q. Yang, and G. Li, *J. Mater. Chem. A* **4**, 12913 (2016).
- [35] X.-H. Cui, X.-H. Li, R.-Z. Zhang, H.-L. Cui, and H.-T. Yan, *Vacuum* **207**, 111615 (2023).
- [36] Y. Zhang, B. Sa, N. Miao, J. Zhou, and Z. Sun, *J. Mater. Chem. A* **9**, 10882 (2021).
- [37] S. Özcan and B. Biel, *Phys. Chem. Chem. Phys.* **25**, 1881 (2023).
- [38] Y. Wang, Y. Tao, Q. Zhang, R. Huang, B. Gao, Z. Li, G. Li, and N. Hu, *Solid State Commun.* **354**, 114893 (2022).
- [39] R. Huang, Y. Wang, C. Li, and C. Dang, *Chalcogenide Lett.* **19** (2022).
- [40] W. Hong, B. C. Wyatt, S. K. Nemani, and B. Anasori, *MRS Bull.* **45**, 850 (2020).
- [41] Z. M. Wong, T. Deng, W. Shi, G. Wu, T. L. Tan, and S.-W. Yang, *Mater. Adv.* **1**, 1176 (2020).
- [42] S. Shaw and S. Ghosh, arXiv:2404.03146 (2024).
- [43] P. E. Blöchl, *Phys. Rev. B* **50**, 17953 (1994).
- [44] G. Kresse and D. Joubert, *Phys. Rev. B* **59**, 1758 (1999).
- [45] G. Kresse and J. Furthmüller, *Comput. Mater. Sci.* **6**, 15 (1996).
- [46] G. Kresse and J. Furthmüller, *Phys. Rev. B* **54**, 11169 (1996).
- [47] J. Heyd, G. E. Scuseria, and M. Ernzerhof, *J. Chem. Phys.* **118**, 8207 (2003).
- [48] S. Baroni, S. De Gironcoli, A. Dal Corso, and P. Gianozzi, *Rev. Mod. Phys.* **73**, 515 (2001).
- [49] A. Togo and I. Tanaka, *Scr. Mater.* **108**, 1 (2015).
- [50] S. Nosé, *J. Chem. Phys.* **81**, 511 (1984).
- [51] M. Gajdos, K. Hummer, G. Kresse, J. Furthmüller, and F. Bechstedt, *Phys. Rev. B Condens.* **73**, 45112 (2006).
- [52] S. Saha, T. Sinha, and A. Mookerjee, *Phys. Rev. B Condens.* **62**, 8828 (2000).
- [53] C. C. McCrory, S. Jung, J. C. Peters, and T. F. Jaramillo, *J. Am. Chem.* **135**, 16977 (2013).
- [54] Y. Zheng, Y. Jiao, M. Jaroniec, and S. Z. Qiao, *Angew. Chem. Int. Ed* **54**, 52 (2015).
- [55] P. Wang, H. Liu, Y. Zong, H. Wen, J.-B. Xia, and H.-B. Wu, *ACS Appl. Mater. Interfaces.* **13**, 34178 (2021).
- [56] J. Bardeen and W. Shockley, *Phys. Rev.* **80**, 72 (1950).
- [57] Z. Jin, X. Li, J. T. Mullen, and K. W. Kim, *Phys. Rev. B* **90**, 045422 (2014).
- [58] Z. Wang, N. Qiu, E. Wu, Q. Huang, P. An, H. He, and S. Du, *J. Mater. Res. Technol.* **24**, 173 (2023).
- [59] E. Prada, J. Alvarez, K. Narasimha-Acharya, F. Bailen, and J. Palacios, *Phys. Rev. B* **91**, 245421 (2015).
- [60] P. Cudazzo, I. V. Tokatly, and A. Rubio, *Phys. Rev. B* **84**, 085406 (2011).
- [61] S. Arra, R. Babar, and M. Kabir, *Phys. Rev. B* **99**, 045432 (2019).
- [62] S. Arra, R. Babar, and M. Kabir, *Phys. Rev. Mater.* **3**, 095402 (2019).
- [63] T. C. Berkelbach, M. S. Hybertsen, and D. R. Reichman, *Phys. Rev. B* **88**, 045318 (2013).